Amorpheus: a Python-based software for the treatment of X-ray scattering data of amorphous and liquid systems

S. Boccato, Y. Garino, G. Morard, B. Zhao, F. Xu, C. Sanloup, A. King, N. Guignot, A. Clark, G. Garbarino, et al.

▶ **To cite this version:**

S. Boccato, Y. Garino, G. Morard, B. Zhao, F. Xu, et al.. Amorpheus: a Python-based software for the treatment of X-ray scattering data of amorphous and liquid systems. High Pressure Research, 2022, 42 (1), pp.69-93. 10.1080/08957959.2022.2032032 . hal-03706916

HAL Id: hal-03706916
https://hal.science/hal-03706916

Submitted on 25 Oct 2022

HAL is a multi-disciplinary open access archive for the deposit and dissemination of scientific research documents, whether they are published or not. The documents may come from teaching and research institutions in France or abroad, or from public or private research centers.

L'archive ouverte pluridisciplinaire **HAL**, est destinée au dépôt et à la diffusion de documents scientifiques de niveau recherche, publiés ou non, émanant des établissements d'enseignement et de recherche français ou étrangers, des laboratoires publics ou privés.

To appear in *High Pressure Research*
Vol. 00, No. 00, Month 20XX, 1–35

Amorpheus: a python-based software for the treatment of x-ray scattering data of amorphous and liquid systems

S. Boccato[1*], Y. Garino[1], G. Morard[2], B. Zhao[1], F. Xu[1,3], C. Sanloup[1], A. King[4], N. Guignot[4], A. Clark[1,5], G. Garbarino[6], M. Morand[1], D. Antonangeli[1]

[1]*Sorbonne Université, Muséum National d'Histoire Naturelle, UMR CNRS 7590, Institut de Minéralogie, de Physique des Matériaux, et de Cosmochimie (IMPMC), 75005 Paris, France*;
[2]*ISTerre, Université Grenoble Alpes, Grenoble, France*;
[3]*Current address: Department of Earth Sciences, University College London, WC1E 6BT London, United Kingdom* ;
[4]*Synchrotron SOLEIL, L'Orme de Merisiers, Saint Aubin-BP48, 91192 Gif-sur-Yvette, France*;
[5]*Current address: University of Colorado, Boulder, Colorado*;
[6]*ESRF - European Synchrotron Radiation Facility, Grenoble, France.*

(*Received 00 Month 20XX; final version received 00 Month 20XX*)

The diffuse scattering signal of amorphous or liquid systems contains information on the local atomic structure, and this can be related to the density, compressibility, thermal expansion and other thermo-elastic properties. However, the analysis and full exploitation of the diffuse scattering signal, in particular for systems under extreme conditions of high pressures and temperatures is difficult to handle.

Amorpheus is a Python-based software allowing the determination of the structure factor and the radial distribution function of amorphous and liquid systems. Based on previously reported methodologies, Amorpheus stands out for the implementation of automatic algorithms allowing the user to choose the most suitable parameters for the data treatment and making possible the systematic analysis of datasets collected in experiments carried out in Paris-Edinburgh press, multi-anvil apparatus or diamond anvil cell.

Keywords: Liquids, amorphous, disordered systems, local structure, software

1. Introduction

Liquid diffuse scattering was observed for the first time in 1916 by Debye and Scherrer [1] and many efforts were devoted to the development of the theory behind this phenomenon [2]. Since then, a considerable work has been done in the quantitative analysis of diffuse scattering data to determine the local structure of disordered and amorphous systems. The standard treatment to obtain the structure factor - S(Q) - and the radial distribution function - g(r) - from the raw x-ray and neutron scattering intensity was presented for the first time by Rahman [3], Warren [4] and Kaplow [5] in the late sixties. Later on, the treatment has been adapted to high-pressure measurements by Sanloup et al. [6] and Eggert et al. [7], extending the analysis of x-ray diffraction to fluids in diamond anvil cell (DAC), and by Funamori et al. [8, 9] for the analysis of energy dispersive x-ray diffraction in large volume presses. More recently, the method has been fully exploited thanks to

*Corresponding authors: silvia.boccato@upmc.fr, yiuri.garino@upmc.fr

the use of a combined angular and energy dispersive x-ray diffraction (CAESAR) technique coupled to large volume presses[10–12]. As today, liquid diffuse scattering have been measured under static and dynamic high-pressure conditions for a large variety of amorphous and liquid systems, be these alloys, mono-atomic, molecular or polymeric systems (e.g. [6, 11, 13–21]) Measurements of S(Q) and g(r) as a function of pressure and temperature allow the determination of compressibility (e.g. [22]) and thermal expansion (e.g. [11]) of liquid systems and the detection of amorphous-amorphous or liquid-liquid phase transitions (e.g. [18, 21, 23–25]). In parallel, the atomic pair distribution function (PDF) method has also been developed, exploiting extremely high X-ray energies and data collection over a large q-range to achieve higher resolution in real space [26, 27].

In view of the large amount of data that it is now possible to collect in synchrotron experiments, the data analysis process calls for a versatile and easy-to-use software that allows systematic approach, including testing the input parameters on a series of data. Currently, many groups analyzing amorphous and liquid diffraction data use home-made codes, not necessarily transparent in their functioning, often requiring the installation of proprietary programs, or some programming skills.

Few are the software packages that provide open-source and free solutions allowing performing an analysis customizable for each experiment: Glassure[28], LiquidDiffract[29], LASDiA [30], PDFgetX3[31] and GudrunX[32]. Among those, Glassure[28], PDFgetX3[31] and GudrunX[32] are optimized for the determination of the atomic pair distribution function but, at their present state, these packages cannot be used to invert for the density. LiquidDiffract[29] and Amorpheus are very similar with respect to the analysis performed with little differences. LiquidDiffract[29] has a graphical user interface that makes it easy-to-use, conversely a systematic analysis and the study of the dependence of the derived quantities on the input parameters cannot be automatically performed (advanced python skills are required to consider using this software as a library). As today, each scattering pattern has to be analyzed individually and a routine allowing the analysis of a set of data does not exist.

Amorpheus has a command-line-based and user-friendly interface that allows efficient navigation of the menus and changing the input parameters with the use of the keyboard only. The S(Q) and g(r) of x-ray scattering intensity data can be computed and exported, with routines and protocols accounting for the sample environment: ambient conditions measurements or high-pressure, high-temperature experiments obtained in a variety of sample environments. Furthermore, best-input parameters can be chosen thanks to automatic algorithms implemented over user-customized ranges. In this way the user has complete control of the choice of the input parameters and can assess those more adapted to find a local minimum in the solution space, as these automatic algorithms allow quickly probing the values of the figure of merit through a loop over user-defined values of the input parameters. A batch analysis on a large set of data is also possible so as to ensure a consistent treatment over the entire data set.

In summary, Amorpheus is an effective alternative to the already existing programs, appealing not only to users who prefer a command-line-based interface, but also to all users who wish to carefully explore the solution space and exploit the possibility to analyze data in batch.

2. Analytical procedure for the treatment of the X-ray scattering of liquids and amorphous systems

The iterative analytical procedure behind the program Amorpheus is based on the methodology originally developed by Kaplow [5], later reformalized by Eggert [7] for

molecular systems, subsequently adapted to metallic systems in [13] and more recently improved in order to reduce the uncertainties caused by the limited range in the scattering vector Q of the function S(Q) [20], a common limitation in high-pressure experiments.

A brief description of the analytical procedure of data treatment for disordered systems is here provided, with the purpose of presenting the equations underlying the program and the used notation (for a more detailed description of the data analysis please refer to [7, 20, 33] as well as the appendix of [22]). The parameters that play a role in the correct determination of S(Q) and g(r) as well as in the estimation of the density are presented. The correspondence between the name of these parameters in the equations and in the code is reported in Appendix 5, where the limits in the parameter space and how these are set in the code are also discussed.

The measured scattering intensity contains contributions from both the sample and its environment (e.g. the diamonds, the pressure transmitting medium, the capsule containing the sample, etc.). The sample's signal I^{sample} is extracted subtracting the contribution of the environment I^{bkg} from the measured signal I^{meas}:

$$I^{sample}(Q) = I^{meas}(Q) - b * I^{bkg}(Q), \tag{1}$$

where b is a scale factor for the background correction, an adimensional parameter that is optimized during the analysis. The scattering vector Q is determined by the scattering angle 2θ and the wavelength of the x-rays λ according to the relation $Q = 4\pi \sin(\theta)/\lambda$. The range in Q where the analysis is performed is user-defined and delimited by the limiting scattering vectors Q_{min} and Q_{max}.

The scattering intensity I^{sample} has a coherent I^{coh} and an incoherent (Compton) I^{incoh} contribution. The incoherent part is the sum of the incoherent scattering signals from the n elements in the sample $\sum_n I_n^{incoh}(Q)$.

2.1. *Faber-Ziman structure factor with Krogh-Moe-Norman normalization*

With the Krogh-Moe-Norman normalization [34], the structure factor $S(Q)$ is obtained as:

$$S(Q) = \frac{\left[\alpha I^{sample}(Q) - \sum_p I^{incoh}(Q)\right] + (< f >^2 - < f^2 >)}{< f >^2} \tag{2}$$

where

$$\alpha = \frac{-2\pi^2\rho_0 + \int_0^{Q_{max}} \frac{\sum_p I^{incoh}(Q) + <f^2>}{<f>^2} Q^2 dQ}{\int_0^{Q_{max}} \frac{I^{sample(Q)}}{<f>^2} Q^2 dQ} \tag{3}$$

Here f is the atomic form factor of constituent elements and $< f^2 >= \sum_n X_n f_n^2(Q)$ and $< f >^2 = \sum_n \sum_m X_n f_n(Q) X_m f_m(Q)$, where X_n is the atomic ratio of n-th element.

Be r the distance with respect to the origin atom, the distribution function $F(r)$ is obtained by a Fourier transform of the structure factor computed iteratively.

At the i-th iteration:

$$F_i(r) = \frac{2}{\pi} \int_0^{Q_{max}} Q(S_i(Q) - 1) \sin(Qr) dQ = 4\pi r[\rho_i(r) - \rho_0] \tag{4}$$

$$g_i(r) = \frac{\rho(r)}{\rho_0} = \frac{F_i(r) + 4\pi r\rho_0}{4\pi r\rho_0} = \frac{\Delta F_i(r)}{4\pi r\rho_0} \tag{5}$$

where $\rho(r)$ is the average atomic density function and ρ_0 is the average density. Tests indicate convergence after 3 iterations. Nonetheless, to ensure convergence, the number of iterations is set to 5 [7].

Due to the steric hindrance, no atoms can be located at a distance from the origin atom below a cutoff radius r_{min}. This implies that at low distances ($r < r_{min}$) $g(r) = 0$ and therefore the value of F(r) has to be as close as possible to $-4\pi\rho_0 r$. This can be expressed as:

$$\forall r < r_{min} \;:\; g_i(r) = 0 \;\rightarrow\; F_i(r) = -4\pi\rho_0 r \;. \tag{6}$$

At the $(i+1)$-th iteration, the $F_i(r)$ at low distances can thus be inverse Fourier transformed and subtracted to the structure factor $S_i(Q)$,

$$S_{i+1}(Q) = S_i(Q)\Big[1 - \frac{1}{Q}\int_0^{r_{min}} \Delta F_i(r)\sin(Qr)dr\Big] \tag{7}$$

This procedure is iteratively repeated allowing to determine S(Q), F(r) and g(r).

In this iterative procedure for the normalization, parameters such as b, Q_{max}, r_{min} and ρ_0 are chosen *a priori*, and the normalization performed for that specific set of parameters.

The average density ρ_0 and the scale factor b can be obtained by minimizing the figure of merit:

$$\chi^2(r_{min}, Q_{max}, \rho_0, b) = \int_0^{r_{min}} [\Delta F(r)]^2 dr. \tag{8}$$

The χ^2 minimization allows the determination of the two aforementioned parameters for each couple of r_{min} and Q_{max}.

In summary, the four parameters to be determined are: ρ_0, b, r_{min} and Q_{max}. Note that an optimum Q_{max} minimizes artefacts at intermediate distances and not only below r_{min} [5]. It is therefore suggested to check the effect of Q_{max} on the normalization after a first minimization of the figure of merit. It should also be noted that the optimum choice of parameters that well minimizes the figure of merit for the density determination is not necessarily the set of parameters that yields the best radial distribution function. Moreover, besides exploring the space of parameters that minimize the figure of merit, it is also recommended, when possible, to test the obtained set of parameters by cross-checking either the derived density ρ_0 or the coordination number of the first coordination shell at conditions at which these are known. For monoatomic materials, the coordination number is obtained according to the relation $N_C = \int_0^{r_M} 4\pi\rho_0 r^2 g(r)dr$. Please note that for polyatomic systems this calculation is not valid and a more complex analysis (at present not implemented in Amorpheus) should be performed [35].

2.2. *Faber-Ziman structure factor with Modification Function*

A main problem in the inversion of diffraction data arises from the limitation in the exploitable scattering angles (limited angular aperture) which directly translates into a limited range in the scattering vector, characterized by a Q_{max} value [36]. A sharp cut in the $S(Q)$ causes artifacts in the form of spurious features in the resulting $F(r)$ and, consequently, in the $g(r)$. A way to overcome this problem is the use of a suitable

modification function $M(Q, \Delta(r))$. In this software we implemented the Lorch function [37] in the form

$$M(Q, \Delta(r)) = \frac{\sin(Q, \Delta(r))}{Q\Delta(r)}, \text{ where } \Delta(r) = \frac{\pi}{Q_{max}}\Big[1 - \exp\Big(-\frac{|r-a|}{b}\Big)\Big] \tag{9}$$

as proposed and discussed in [38]. Provided a suitable choice of input parameters (see Appendix 5) at the last iteration the structure factor is multiplied by the modification function and Equation 4 becomes:

$$F(r) = \frac{2}{\pi}\int_0^{Q_{max}} M(Q, \Delta(r))Q(S_5(Q) - 1)\sin(Qr)dQ \ . \tag{10}$$

It has to be noted that the use of a modification function allows for the extraction of a smooth g(r) but does not affect the resulting value of the density.

3. Software structure

The Amorpheus software was conceived to treat x-ray scattering data of liquid and amorphous systems at ambient conditions as well as at high pressure and temperature. It is designed to be compatible with both laboratory and synchrotron data collected with a wide variety of high-pressure devices such as diamond anvil cell (DAC), multi anvil (MA) and Paris-Edinburgh (PE) press. Amorpheus can treat data collected with angle dispersive x-ray diffraction as well as the CAESAR technique [11, 12] that combines angular and energy dispersive X-ray diffraction. Here below is presented the general structure of the program, followed by how it is distributed and the dependencies it relies on.

The software's functional flowchart is represented in Figure 1. White and gray shaded background represented two main parts of the program: Amorpheus and Remove Peaks and Smooth (RPS), respectively. Amorpheus allows to obtain the structure factor S(Q), the radial distribution function g(r) and the density ρ_0, while RPS can be used for pre-treating of raw data.

[*Figure 1 near here*]

3.1. *Amorpheus*

As schematized in Figure 1, Amorpheus software allows treating the data and specifically: remove the background, normalize the signal to atomic units calculating the structure factor, optimize the parameters obtaining the density ρ_0 that minimizes the figure of merit, and determine the radial distribution function $g(r)$ of the liquid or the amorphous system under analysis. Input parameters are defined in the file 'Init.txt'. An exhaustive description of the input parameters is provided in Appendix 5. When running the program, the menu appears as shown in the bottom portion of Figure 1. The different sections of the menu are:

Visualize [v] This section of the menu plots the raw data over the full range before any treatment. The conversion from the data in 2θ (as in File Format 1 and 2, see Appendix 5) and from Q in $\mathring{A}^{-1}$ (as in File Format 3 and 4, see Appendix 5) to Q in nm^{-1} is directly visualized in the plot with the help of a double x axis.

Normalize [n] Here it is possible to normalize the input scattering intensity to atomic units in order to obtain the structure factor and the radial distribution function for defined parameters r_{min}, Q_{min}, Q_{max}, b and ρ_0. The Faber-Ziman structure factor [39] is calculated with a Krogh-Moe-Norman normalization [34] as shown in Equations 2 and 3. This choice is well suited for materials in the amorphous or liquid state. This operation was tested on a DELL Latitude E5490 (laptop used for all benchmark timings quoted below) with the integrals in Equations 4 and 7 explicitly calculated using the trapezoidal rule implemented in the library numpy[40]. An example of normalization results is shown in Figure 2.

A choice of the input parameter Normalization = 1 (see Appendix 5), allows the optional use of a modification function described in Equation 9, and applied to the structure factor at the 5th and last iteration (see Figure 3).

[*Figure 2 near here*]
[*Figure 3 near here*]

Loop over rmin [r] and **Loop over qmax [x]** In these sections the figure of merit of Equation 8 is minimized through optimization of the density and scale factor parameters. The value of the figure of merit (χ^2 of Equation 8) depends on the cutoff radius r_{min} and the Q_{max}. A loop over these two parameters, independently treated in the two sections, allows to find the values that best minimize the figure of merit, and the associated density. An example is provided in Figure 4 and 5. The shown loop on 25 values of qmax took about 30 minutes (on a DELL Latitude E5490).

[*Figure 4 near here*]
[*Figure 5 near here*]

Batch [b] This section of the program allows treating a set of data. In this case the input parameters have to be defined in a file named Batch.ods. For each file the density and the scale factor are minimized for the same selected cutoff distance r_{min}. The obtained density and scale factor are then used to normalize the data and obtain, after 5 iterations, the $S(Q)$ and the $g(r)$. An example of batch minimization is shown in Section 4.3.

χ^2 **[c]** A contour plot of the figure of merit in the ρ_0-scale factor space (when there is a background signal) can be calculated and shown to check for independence of the two parameters. An example of χ^2 contour plot is shown for Ce-based glass in Section 4.1, Figure 7. This calculation can be very time consuming, depending on the required precision for the mesh. A calculation with 100x100 points can take about 2 hours (on a DELL Latitude E5490).

Parameters [p] This section of the program allows changing the input parameters for the analysis. The complete list of parameters is shown in Appendix 5, where their use and their range of validity is shown.

3.2. *RPS*

The Remove Peaks and Smooth (RPS) is an independent tool that can be used in support of the main software Amorpheus to pre-treat the data.

[*Figure 6 near here*]

With its graphical interface, RPS allows to remove the eventual remaining peaks of a solid phase in coexistence with the liquid, or coming from the environment and hiding the liquid signal. For example, these can originate from the solid pressure-transmitting

medium embedding the liquid sample and not filtered by multichannel collimators [41, 42]. The RPS software allows to easily remove undesired peaks through a fit to a Lorentz a Gaussian or a Voigt distribution function with a linear background. The peak can also be removed erasing the data in the selected range. In some cases the peak to remove can be very intense and/or have a shape different from the chosen profile: in this case peak removal will leave a non-smooth function in place of the solid peak. An example is shown in Figure 6. The raw data are shown in black, in the left side of the window, the range in 2θ between 8.935° and 9.751° has been chosen for peak removal. This very intense solid peak is not perfectly described by the chosen analytical shape and the signal with the peak subtracted does not look perfectly smooth in the fit region. For this reason the Smooth function [43] has been introduced to RPS. The curve in green is the signal after smoothing, which faithfully reproduces the features of the liquid signal, but removes the artifacts due to the peak removal, as it is visible for the peak at 16°.

3.3. *Distribution and dependencies*

Amorpheus is an open source software and it can be downloaded from https://github.com/CelluleProjet/Amorpheus [1]. Step by step installation instructions are also provided in the same webpage. Amorpheus was conceived to be used on the development environment Spyder (https://www.spyder-ide.org/) and it makes a large use of several existing libraries that are available on Anaconda (https://anaconda.com), such as numpy [40] and scipy [44] for numerical operations, matplotlib [45] for plotting data, xraylib [46] for the form factors of various elements and lmfit [47] for the optimization of the figure of merit.

The RPS graphical user interface is based on the standard tkinter package [48]. Upon request, an executable package can be provided via email.

Currently, Amorpheus has been tested on Windows 10, Ubuntu 20.04 and Mac OS X.

4. Application to real data and benchmark

Several examples out of actual experimental activity, either from us or from recent literature, are here presented. Discussed data have been measured on different synchrotron beamlines and with different sample environments (see Table 1). The first three examples are data obtained by angle dispersive x-ray diffraction experiments performed on beamline ID27 at the ESRF in a diamond anvil cell, with and without the multichannel collimator [41, 42]. In these cases, the sample's signal is extracted by subtracting the background from the collected data. The following three examples are data collected on the diffraction beamline PSICHE at SOLEIL by CAESAR technique, which combines angular and energy dispersive geometry [11, 12]. The CAESAR technique allows exploring a wide range in Q and effectively minimizing the background. These examples were chosen irrespectively of the specific scientific interest, but rather to highlight the versatility of the program and its capability in different high pressure and temperature conditions.

[*Table 1 near here*]

[1] A DEMO version of the software can temporarily be found in:
https://www.dropbox.com/sh/t5uds7wo13371z1/AACpgRKBmLzrzlu8vVyUAtWua?dl=0

4.1. *Cerium-based glass*

Examples of X-ray scattering data collected for a Cerium-based glass ($Ce_{70}Al_{10}Ni_{10}Cu_{10}$) were used in Section 3.1 to show the different parts of the software. These high-quality XRD measurements [14, 49] have been performed in DAC at ∼1 GPa on the ID27 beamline of the ESRF synchrotron.

These data, in the form of scattering intensity as a function of the scattering vector Q, and from which a background has to be subtracted, are an example of File Format = 4 (see Appendix 5).

The choice of optimal input parameters was performed using the **Loop over rmin [r]** and **Loop over qmax [x]**, shown as examples in Figures 4 and 5 in Section 3.1. The density obtained in this work (34.68 at/nm^3) is within 3% of the density measured at ambient pressure for $Ce_{70}Al_{10}Ni_{10}Cu_{10}$ amorphous compound (35.6 at/nm^3) [50]. Note that being the bulk modulus of this Ce-based glass 27 GPa [51], the expected density difference between ambient pressure and 1 GPa is negligible. Thus, this 3% difference will be hereafter considered to be the uncertainty on the density obtained by this analysis.

Comparison of S(Q) (already shown in Figure 2) with literature results [52] is reported in the left panel of Figure 7. The very good agreement, in particular concerning the location of the local maxima in the S(Q), validates the present approach and analysis.

The χ^2 contour plot for the Ce-based glass is shown in the right panel of Figure 7 in the ρ_0-b space. The circular symmetry around the minimum of the χ^2 demonstrates the independence of density and scale factor [7].

[*Figure 7 near here*]

4.2. *Liquid Fe*

X-ray scattering measurements on liquid iron were collected on the ID27 beamline at the ESRF. High pressure and high-temperature conditions were generated by means of a diamond anvil cell heated from both sides by two YAG infrared lasers focused on a 20x20 μm^2 region of the sample. Pressure was determined using the thermal equation of state (EoS) of the KCl pressure-transmitting medium [53]. The temperature of KCl was assumed to be a weighted average between the temperature measured at the surface of the sample and the temperature of the diamond (300 K), as proposed in [54].

[*Figure 8 near here*]

Monochromatic X-rays with a wavelength of 0.3738 $\AA$ were focused down to a 3x3 μm^2 spot at the center of the heated portion of the sample, and X-ray scattering was collected on a MAR CCD detector (5 seconds integration time). The sample, a 10 μm thick 99.99% pure foil from Goodfellow, was heated for slightly longer than 5 seconds, over a temporal window encompassing the x-ray scattering collection. This relative short integration and heating time is the outcome of a compromise between a good enough signal to noise ratio and the necessity to avoid temperature-triggered chemical reactions. The temperature was obtained by fitting to a Plank law the gray body emission collected from a 2×2μm^2 area at the center of the hotspot. Appearance of liquid diffuse scattering and disappearance of sharp peaks from solid iron were taken as melting criteria. XRD peaks coming from KCl surrounding the sample were removed thanks to the RPS pre-treatment tool described in Section 3.2 (in Figure 6).

The background extracted using the program Dioptas [55] from the last solid XRD pattern before melting (i.e. at the highest available temperature) is used as background in the analysis of the XRD signal from the liquid.

The structure factor and radial distribution function for liquid iron at 38±2 GPa and 3400±300 K are shown in the top panels of Figure 8. While position of q1 = 31.8 nm^{-1} is clear and in good agreement with the literature [33, 56], the position of q2 is difficult

to localize due to the presence of spurious signal. The comparison of the here-derived g(r) to the one obtained by Kuwayama et al. [20] shows that the obtained positions are very comparable (see Figure 8), even if the intensity of the peaks is slightly different. The obtained density of 87±3 at/nm^2 is also compared to the thermal equation of state by Kuwayama et al. [20]. Once considering all uncertainties (the uncertainties of the literature equation of state and on the temperature are not shown in the bottom panel of Figure 8), the here-derived density is in fare agreement with the value expected according literature.

4.3. *Amorphous $MgSiO_3$*

Data collected on amorphous $MgSiO_3$ at high pressure are used to present an application of the batch analysis implemented in the Batch part of the program. Diffuse scattering on amorphous $MgSiO_3$ were recorded from 2 to 81 GPa on the XRD beamline ID27 at the ESRF using multichannel collimators [41, 42]. High pressure was obtained with a membrane driven DAC. $MgSiO_3$ was placed in a pre-indented gasket together with a small piece of KCl that was used as pressure calibrant [53]. The background signal was measured on the empty cell. Further experimental details for this experiment are presented in [19].

The input parameters for the batch analysis were chosen by checking ahead few scattering signals at different pressures. Input parameters for the intermediate pressures were then defined accordingly. We performed and compared three batch analysis, with the same input parameters but on data pre-treated with different smoothing protocols (see Section 3.2): results obtained on the raw data (hereafter referred to as unsmoothed data) and on data with smoothing parameter 50 and 100.

The densities obtained as a function of pressure for the three sets of data are shown in the left panel of Figure 9. Values are within mutual uncertainties, indicating that the smoothing of the data does not affect the derived densities, which are in very good agreement with literature results by absorption measurements [57]. The effect of the smoothing on the S(Q) is shown in the right panel of Figure 9. Here, the S(Q) obtained in this work at 27 GPa is compared to the one reported in the literature at 30 GPa [58].

[*Figure 9 near here*]

[*Figure 10 near here*]

The evolution with pressure of the structure factor and the radial distribution function is shown in Figure 10 for selected pressures in the investigated range. The first two peaks in the S(Q) are indicated as q1 and q2. As expected for a general compression of the system, both q1 and q2 shift to higher values with increasing pressure, however, while the intensity of peak q1 decreases with pressure, the q2 structure becomes more clear and intense. These results are in qualitative agreement with previous x-ray diffraction measurements performed over a comparable range [58]. The decrease of q1 and increase of q2 peak intensity concomitant to the shift of the peaks position to higher Q was also observed in neutron total structure factors reported up to 20 GPa [59], but the relative intensities of q1 and q2 as a function of pressure obtained by x-ray and by neutrons cannot be directly compared.

The first and second peak in the radial distribution function are indicated as r1 and r2, respectively. As reported in Kono et al.[58], peak r1 corresponds to the average Si-O distance [60] and this becomes larger with increasing pressure as a consequence of the increase of coordination number of Si from 4 to 6. Peak r2 corresponds instead to the average Si-Si distance, which decreases with pressure due to compression. The positions of the maxima for peak r1 and r2 as a function of pressure are reported in the bottom panel of Figure 10, where they are compared with literature results [58]. The trends are

qualitatively comparable, the only difference being the absolute values, that were tested to be related to the differences in the covered Q ranges in the two studies.

4.4. *SiO_2 glass*

X-ray diffraction data obtained on SiO_2 glass are used to present the application of the modification function, described in Section 2.2. X-ray scattering measurements were performed with the CAESAR technique [11, 12] on the beamline PSICHE at SOLEIL. A sapphire capsule for Paris-Edinburgh press experiments was filled with compacted powder of SiO_2. The measurement was performed at ambient conditions.

Data were collected as Intensity as a function of scattering vector Q, with a high degree of redundancy possible thanks to the CAESAR method. Therefore, a fitting process to calculate the effective incident beam spectrum similar to that described in [61] can be used to normalize the data and produce a single spectrum. A background can be collected under the same conditions and subtracted if needed. However, due to the high degree of collimation of the detected beam this is usually an unnecessary correction, except for samples whose volume is very small compared to the probed volume. In the example shown here, data were analyzed without background extraction as implemented in the File Format = 3.

Structure factor and radial distribution function obtained by normalization with rmin = 0.122 nm and $\rho_0 = 66$ at/nm^3 [15, 62] are shown in Figure 11. Spurious oscillations in the g(r) were removed with the application of the modification function M(Q,Δ(r)) (Equation 9), choosing parameters a = 0.16 nm and b = 0.05 nm. The peaks positions for both the S(Q) and the g(r) with modification function are indicated in the caption of Figure 11. The comparison of the obtained S(Q) with previously published results [15, 63, 64] highlights a good agreement both in the position of the peaks and in the relative peak intensities. The g(r) before application of the modification function is in good agreement with Funamori et al. and Kono et al. [63, 64], but the best agreement for the g(r) is obtained with the results of Prescher et al. [15].

[*Figure 11 near here*]

4.5. *Liquid Al*

X-ray diffraction data for liquid aluminum considered here have been obtained by CAESAR technique [11, 12] on the PSICHE beamline at Synchrotron SOLEIL. The analysis was performed using the Batch function of the program with Normalization Type = 1 that allows the use of the Modification Function on the resulting g(r). The considered data were collected under simultaneous high-pressure and high-temperature conditions, up to 2 GPa and 1350 K. These conditions were achieved thanks to the UToPEC (Ultrafast Tomography Paris Edinburgh Cell) [65, 66]. The sample, a GoodFellow (99.9% pure) Aluminum cylinder 0.5 mm high and with a diameter of 1 mm, was embedded in a hBN capsule, surrounded by a graphite heater and loaded in a 7/2.4 assembly for the Paris-Edinburgh press using boron epoxy as pressure medium. The graphite heater is connected to a DC power supply. The power-temperature calibration was obtained on a test run using a mixture of hBN, Pt and MgO and by cross calibrating their EOS [67–69]. The thermal EOS of hBN was then used to obtain the pressure [67].

[*Figure 12 near here*]

[*Table 2 near here*]

S(Q) and g(r) for the measured signals are shown in Figure 12. The modification function was applied to the data, with a = 0.28 nm and b = 0.05. Peak positions for the S(Q) and the g(r) of the two signals are reported in Table 2. The differences in the

pressure and temperature conditions are small enough not to significantly affect the the peak positions of the S(Q), while the intensity of q1 slightly decreases from 2.46 (at 1.5 GPa and 1200 K) to 2.38 (at 2 GPa and 1350 K). Both observations are in good agreement with what reported in the literature [70] for similar measurements under similar thermodynamic conditions. For the S(Q), the peaks' position in the derived g(r) is not affected by the little differences in pressure and temperature, while the r1 peak intensity decreases from 2.87 (at 1.5 GPa and 1200 K) to 2.82 (at 2 GPa and 1350 K). This is in agreement with results from molecular dynamics calculations performed at ambient pressure for temperatures between 875 and 1250 K [71]. Specifically, calculations indicate that the position of the r1 peak does not change with the temperature (computed absolute value is only 5 pm lower than our experimental determination, well within the uncertainties) while its intensity lowers from 2.96 at 875 K to 2.59 at 1250 K. The coordination number obtained according to the relation $N_C = \int_0^{r_M} 4\pi\rho_0 r^2 g(r) dr$, where r_M is the first minimum in the g(r), is 11.39 at 1.5 GPa and 1200 K and 11.24 at 2 GPa and 1350 K. This decrease in the coordination number is also compatible with calculations at high pressure presented in Jakse et al.[71] and the molecular dynamics simulations by Gonzalez et al.[72], where at ambient pressure the coordination number decreases by 1.3 each 1000 K.

[*Figure 13 near here*]

The density was minimized in the Q range 6 - 110 nm^{-1}. The values of rmin were determined finding local minima in the figure of merit using the **Loop over rmin [r]** function of the program described in Section 3.1. The best rmin for 1.5 GPa and 1200 K data is 0.216 nm, and the minimized density is 52.32 at/nm^3. The best rmin for 2 GPa and 1350 K data is 0.214 nm, with a minimized density of 52.03 at/nm^3. These results are shown in Figure 13, where they are compared with the high-temperature 2nd-order Birch-Murnaghan equation of state reported by Ikuta et al.[70] at temperatures of 1373, 1573 and 1773 K and here recalculated for 1200 and 1350 K. Within the uncertainties, our results are in good agreement with the literature.

4.6. *Liquid Fe-Si*

Here we present the structure factor, radial distribution function (top panel of Figure 14) and density of a liquid Fe-Si alloy containing 32.5±0.8 at% Si (as determined by the Cameca SX100 electron microprobe at CAMPARIS, Sorbonne Université) at 7.3 GPa and 1990 K measured combining angular and energy dispersive X-ray diffraction (CAESAR) technique on the beamline PSICHE at Synchrotron SOLEIL, France. [11]. High pressure high-temperature experiments were performed using a DIA-type multi-anvil press. As illustrated in Figure 14, the derived local structure is in good agreement with previous experimental [73] and numerical [52] studies.

[*Figure 14 near here*]

The minimized density obtained in the Q range 10-100 nm^{-1} and with rmin = 0.176 is 79.2±2.0 at/nm^3 (6164 kg/m^3). This value is in closer agreement with early density determination by x-ray absorption technique [74] than subsequent estimation obtained by sink-float method [75]. A more complete analysis is required, but differently from what suggested by Tateyama et al. [75], our preliminary results suggests that an ideal mixing between Fe and Si end-member well accounts for the density of the liquid Fe-Si alloys.

4.7. *Future developments*

The implementation of the Ashcroft-Langreth structure factor [76] as an alternative to the Faber-Ziman structure factor is ongoing. This choice can be more suited for poly-atomic molecular systems [7].

Further planned development in the short term includes the implementation of the prolongation of $S(Q)$ following an approach similar to what recently used for the analysis of the structure of liquid iron [20].

Moreover we are willing to implement a test on low Q prolongation of the S(Q), checking in which cases the limit

$$\lim_{Q\to 0} S(Q) = S(0) = \rho_0 K_B T \beta$$

can be exploited to auto-consistently check the density determination, where k_B is the Boltzmann constant, β the isothermal compressibility and T the absolute temperature. Note that this method already gave promising results for molten fayalite [77].

5. Conclusions

We developed the Amorpheus software with the goal to provide a versatile tool for the analysis of x-ray diffuse scattering signal, which allows obtaining the structure factor, the radial distribution function and the density for liquid and amorphous solid systems.

The user-friendly, interactive and command-line-based interface allows efficient test of input parameters, important both for an improved reliability of the results, both to consistently analyze a large set of data.

Close collaboration with PSICHE beamline will allow users to benefit right away of the last version of the software, but will also help increasing the community using this software. Following the same logic, we are constantly exchanging with beamline scientists across the world and responsibles of laboratory-based x-ray diffraction platforms. At the time of writing Amorpheus is employed by users who collected data on the PSICHE beamline at SOLEIL, the ID27 beamline at ESRF, the I15 beamline at DIAMOND LIGHT SOURCE and at the 13-IDD beamline at APS.

Appendix A. Input parameters

An example of input file 'Init.txt' is shown in the box in Table 3 for the case of the Ce-based glass presented in this work. The values of all input parameters can be changed also in the section **Parameters [p]** of the menu. [*Table 3 near here*]

[1]-[2] **Filename - Filename background:** These parameters are the names of measured I^{meas} and I^{bkg}, respectively. The I^{bkg} is pertinent only if the File Format supports a background. Columns have to be separated by space or tab (files with comma separated columns will not work).

[3] **File Format:** Allows to chose four possible file formats:
- File Format = 1 : data are in 2θ and there is no background
- File Format = 2 : data are in 2θ with a background in the same units
- File Format = 3 : data are in Q in $\mathring{A}^{-1}$ with no background
- File Format = 4 : data are in Q in $\mathring{A}^{-1}$ with a background in the same units

[4] **incoherent:** The parameter of incoherence is set to 1 when the background was measured on the empty cell, as in the case of Cerium glass represented in Table 3 and to 0

when the background was measured on the sample as in the case of iron presented in Section 4.2. In this case the sum of the incoherent scattering signals from the sample is already subtracted while subtracting the background, and in the normalization in Equations 7 and 3 the term $\sum_p I_p^{incoh}(Q)$ is set to 0.

[5] **lambd:** It is the wavelength λ of x-rays expressed in nm. The software reads this parameter only in case of File Format = 1 and 2, when the conversion from angle 2θ to scattering vector Q is performed as $q = \frac{4\pi}{\lambda} \sin\left(\frac{\pi}{180}\frac{2\theta}{2}\right)$. In the case of Cerium shown in Table 3 and in Section 4.1 parameter lambd is set to 1 as the File Format is 4 and this value is not used. In the case of liquid iron presented in Section 4.2 this parameter was set to lambd = 0.03738.

[6]-[7] **qmin - qmax:** Parameters qmin and qmax are the limits for the Q range under analysis, they always have to be expressed in Q even with File Format = 1 and 2. The value of Q_{min} has to be chosen reasonably lower than the position of the diffuse scattering peak, its precise value has little effect in locating the peaks of the radial distribution function. At the first iteration, as in Equation 2, $S(Q)$ is defined between Q_{min} and Q_{max}, but for the aforementioned reason it is typically extrapolated at low Q as $S(Q) = S(Q_{min}), \forall Q, 0 < Q < Q_{min}$. A thorough choice of Q_{max} is instead significant in the minimization of the figure of merit of Equation 8. The **Loop over qmax [x]** section of the software helps in the choice of Q_{max}, Section 3.1.

[8] **rmin:** The choice of the cutoff radius r_{min} is also crucial for the optimization of the figure of merit of Equation 8. This value can be chosen with the help of the **Loop over rmin [r]** section of the software. This value can take on positive values lower than 0.4 nm.

[9] **bkfactor:** The bkfactor parameter is the scale factor b of Equation 1. Its value, at the beginning set to 1, is optimized in the minimization of the figure of merit of Equation 8. In the optimization this value can take on values between 0.7 and 1.2.

[10] **rhomi:** The value of the atomic density ρ_0 is also optimized during the minimization procedure. It is expressed in at/nm^3 and during the optimization it can take on values between -50 and +50 at/nm^3 with respect to the initial set value.

[11] **Normalization Type:** If set to 1, leads to the use of the modification function described in 2.2. When Normalization Type = 0 the standard normalization described in Section 3.1 is performed.

[12] **SofQ:** If set to 1, at the first iteration $S(Q) = S(Q_min)$ for $Q <Q_{min}$. If set to 0, at the first iteration $S(Q) = 0$ for $Q <Q_{min}$. The analyses shown in this work are performed with SofQ = 1.

[13] **QStep:** This parameter currently has to be set to 0 (it will be useful in future developments of the software).

[14]-[16] **Save filenames:** Parameters for saving figures and files associated to **Normalize [n]**, **Loop over rmin [r]** and **Loop over qmax [x]** respectively.

[17]-[18] **Elements - Content:** It is possible to consider systems with up to 6 elements and it is sufficient to type the element symbol in parameter [17] with the corresponding content in at% in the following line [18]. A check that the sum of the element's content is 1 (100%) is performed in the software.

Acknowledgements

The authors are grateful to Eglantine Boulard, Nicki C. Siersch, Laura Henry, Marzena A. Baron, Paraskevas Parisiades, Denis Andrault, Mohamed Mezouar, Jeroen Jacobs, Nicolas Rividi and Michel Fialin for their help during the diffraction experiments, the microprobe analysis and for fruitful discussions. The authors would like to thank Carlo

Boccato for suggesting the name of this software.

The authors acknowledge the European Synchrotron Radiation Facility (ESRF) for provision of beamtime under proposals ES560, HC3943. The authors acknowledge Synchrotron SOLEIL for provision of beamtime under proposals 20171307 and 20191835. This project has received funding from the European Research Council (ERC) under the European Union's Horizon 2020 research and innovation programme (Grant agreement No. 724690).

Declaration of interest statement

The authors declare no competing interests.

References

[1] Scherrer P. Debye, P. Interferenzen an regellos orientierten teilchen im röntgenlicht. i. *Nachrichten von der Gesellschaft der Wissenschaften zu Göttingen, Mathematisch-Physikalische Klasse*, 1916:1–15, 1916.

[2] G. C. Danielson. *X-ray diffraction in liquids*. University of British Columbia., 1935.

[3] Aneesur Rahman. Normalization of diffraction data from liquids. *The Journal of Chemical Physics*, 42(10):3540–3542, 1965.

[4] Warren. *X-Ray Diffraction*. Addison-Wesley, Reading, MA, 1969.

[5] Roy Kaplow, S. L. Strong, and B. L. Averbach. Radial density functions for liquid mercury and lead. *Phys. Rev.*, 138:A1336–A1345, May 1965.

[6] C Sanloup, F Guyot, P Gillet, G Fiquet, R J Hemley, M Mezouar, and I Martinez. Structural changes in liquid Fe at high pressures and high temperatures from synchrotron X-ray diffraction. *Europhys. Lett.*, 52(2):151–157, 2000.

[7] Jon H. Eggert, Gunnar Weck, Paul Loubeyre, and Mohamed Mezouar. Quantitative structure factor and density measurements of high-pressure fluids in diamond anvil cells by x-ray diffraction: Argon and water. *Physical Review B*, 65(17):174105, apr 2002.

[8] Nobumasa Funamori and Kazuhiko Tsuji. Structural transformation of liquid tellurium at high pressures and temperatures. *Phys. Rev. B*, 65:014105, Dec 2001.

[9] Nobumasa Funamori and Kazuhiko Tsuji. Pressure-induced structural change of liquid silicon. *Phys. Rev. Lett.*, 88:255508, Jun 2002.

[10] Yanbin Wang, Takeyuki Uchida, Robert Von Dreele, Mark L. Rivers, Norimasa Nishiyama, Ken-ichi Funakoshi, Akifumi Nozawa, and Hiroshi Kaneko. A new technique for angle-dispersive powder diffraction using an energy-dispersive setup and synchrotron radiation. *Journal of Applied Crystallography*, 37(6):947–956, Dec 2004.

[11] F. Xu, G. Morard, N. Guignot, A. Rivoldini, G. Manthilake, J. Chantel, L. Xie, A. Yoneda, A. King, E. Boulard, S. Pandolfi, F.J. Ryerson, and D. Antonangeli. Thermal expansion of liquid fe-s alloy at high pressure. *Earth and Planetary Science Letters*, 563:116884, 2021.

[12] A. King, N. Guignot, G. Morard, A. Clark, and J.-P. Itie. Combined angular and energy dispersive data analysis: Optimised data acquisition, normalisation, and reduction. in preparation.

[13] Guoyin Shen, Mark L. Rivers, Stephen R. Sutton, Nagayoshi Sata, Vitali B. Prakapenka, James Oxley, and Kenneth S. Suslick. The structure of amorphous iron at high pressures to 67 GPa measured in a diamond anvil cell. *Physics of the Earth and Planetary Interiors*, 143(1-2):481–495, 2004.

[14] G. Morard, G. Garbarino, D. Antonangeli, D. Andrault, N. Guignot, J. Siebert, M. Roberge, E. Boulard, A. Lincot, A. Denoeud, and S. Petitgirard. Density measurements and structural properties of liquid and amorphous metals under high pressure. *High Pressure Research*, 34(1):9–21, 2014.

[15] Clemens Prescher, Vitali B. Prakapenka, Johannes Stefanski, Sandro Jahn, Lawrie B. Skinner, and Yanbin Wang. Beyond sixfold coordinated Si in SiO2 glass at ultrahigh pres-

sures. *Proceedings of the National Academy of Sciences of the United States of America*, 114(38):10041–10046, 2017.

[16] G. Morard, Y. Nakajima, D. Andrault, D. Antonangeli, A. L. Auzende, E. Boulard, S. Cervera, A. N. Clark, O. T. Lord, J. Siebert, V. Svitlyk, G. Garbarino, and M. Mezouar. Structure and density of fe-c liquid alloys under high pressure. *Journal of Geophysical Research: Solid Earth*, 122(10):7813–7823, 2017.

[17] G Morard, S Boccato, A Rosa, S Anzellini, F Miozzi, L Henry, G Garbarino, M Mezouar, M Harmand, F Guyot, E Boulard, I Kantor, T Irifune, and R Torchio. Solving controversies on the iron phase diagram under high pressure. *Geophysical Research Letters*, 45:11, 074 – 11, 082, 2018.

[18] R. Briggs, M. G. Gorman, S. Zhang, D. McGonegle, A. L. Coleman, F. Coppari, M. A. Morales-Silva, R. F. Smith, J. K. Wicks, C. A. Bolme, A. E. Gleason, E. Cunningham, H. J. Lee, B. Nagler, M. I. McMahon, J. H. Eggert, and D. E. Fratanduono. Coordination changes in liquid tin under shock compression determined using in situ femtosecond x-ray diffraction. *Applied Physics Letters*, 115(26):264101, 2019.

[19] Guillaume Morard, Jean-Alexis Hernandez, Marco Guarguaglini, Riccardo Bolis, Alessandra Benuzzi-Mounaix, Tommaso Vinci, Guillaume Fiquet, Marzena A. Baron, Sang Heon Shim, Byeongkwan Ko, Arianna E. Gleason, Wendy L. Mao, Roberto Alonso-Mori, Hae Ja Lee, Bob Nagler, Eric Galtier, Dimosthenis Sokaras, Siegfried H. Glenzer, Denis Andrault, Gaston Garbarino, Mohamed Mezouar, Anja K. Schuster, and Alessandra Ravasio. In situ x-ray diffraction of silicate liquids and glasses under dynamic and static compression to megabar pressures. *Proceedings of the National Academy of Sciences*, 117(22):11981–11986, 2020.

[20] Yasuhiro Kuwayama, Guillaume Morard, Yoichi Nakajima, Kei Hirose, Alfred Q.R. Baron, Saori I. Kawaguchi, Taku Tsuchiya, Daisuke Ishikawa, Naohisa Hirao, and Yasuo Ohishi. Equation of State of Liquid Iron under Extreme Conditions. *Physical Review Letters*, 124(16):165701, 2020.

[21] Laura Henry, Mohamed Mezouar, Gaston Garbarino, David Sifré, Gunnar Weck, and Frédéric Datchi. Liquid-liquid transition and critical point in sulfur. *Nature*, 584:382–386, 2020.

[22] G. Morard, J. Siebert, D. Andrault, N. Guignot, G. Garbarino, F. Guyot, and D. Antonangeli. The earth's core composition from high pressure density measurements of liquid iron alloys. *Earth and Planetary Science Letters*, 373:169–178, 2013.

[23] Srikanth Sastry and C. Austen Angell. Liquid liquid phase transition in supercooled silicon. *Nature Materials*, 2:739–743, 2003.

[24] M. H. Bhat, V. Molinero, E. Soignard, V. C. Solomon, S. Sastry, J. L. Yarger, and C. A. Angell. Vitrification of a monatomic metallic liquid. *Nature*, 448(7155):787–790, 2007.

[25] A. Cadien, Q. Y. Hu, Y. Meng, Y. Q. Cheng, M. W. Chen, J. F. Shu, H. K. Mao, and H. W. Sheng. First-order liquid-liquid phase transition in cerium. *Phys. Rev. Lett.*, 110:125503, Mar 2013.

[26] Simon J. L. Billinge. The rise of the x-ray atomic pair distribution function method: a series of fortunate events. *Philosophical Transactions of the Royal Society A: Mathematical, Physical and Engineering Sciences*, 377(2147):20180413, 2019.

[27] Marion Louvel, James W. E. Drewitt, Allan Ross, Richard Thwaites, Benedict J. Heinen, Dean S. Keeble, Christine M. Beavers, Michael J. Walter, and Simone Anzellini. The HXD95: a modified Bassett-type hydrothermal diamond-anvil cell for *in situ* XRD experiments up to 5 GPa and 1300 K. *Journal of Synchrotron Radiation*, 27(2):529–537, Mar 2020.

[28] Clemens Prescher. Glassure: An API and GUI program for analyzing angular dispersive total X-ray diffraction data, September 2017.

[29] Benedict Johannes Heinen. Liquiddiffract v1.0.0, December 2019.

[30] Francesco Devoto. https://github.com/cicciodevoto/LASDiA/blob/master/LASDiA.py.

[31] P. Juhás, T. Davis, C. L. Farrow, and S. J. L. Billinge. *PDFgetX3*: a rapid and highly automatable program for processing powder diffraction data into total scattering pair distribution functions. *Journal of Applied Crystallography*, 46(2):560–566, Apr 2013.

[32] Alan K. Soper. Gudrunn and gudrunx : programs for correcting raw neutron and x-ray diffraction data to differential scattering cross section. *Rutherford Appleton Laboratory Technical Reports*, 2011.

[33] Guoyin Shen, Vitali B Prakapenka, Mark L Rivers, and Stephen R Sutton. Structure of liquid iron at pressures up to 58 GPa. *Physical Review Letters*, 92(18):185701–1, 2004.

[34] J. Krogh-Moe. A method for converting experimental X-ray intensities to an absolute scale. *Acta Crystallographica*, 9(11):951–953, Nov 1956.

[35] David Pickup, Robert Moss, and Robert Newport. *NXFit*: a program for simultaneously fitting X-ray and neutron diffraction pair-distribution functions to provide optimized structural parameters. *Journal of Applied Crystallography*, 47(5):1790–1796, Oct 2014.

[36] Jürg Waser and Verner Schomaker. The Fourier Inversion of Diffraction Data. *Reviews of Modern Physics*, 25(3):671–690, jul 1953.

[37] E. Lorch. Neutron diffraction by germania, silica and radiation-damaged silica glasses. *Journal of Physics C: Solid State Physics*, 2(2):305, feb 1969.

[38] Lawrie B. Skinner, Congcong Huang, Daniel Schlesinger, Lars G. M. Pettersson, Anders Nilsson, and Chris J. Benmore. Benchmark oxygen-oxygen pair-distribution function of ambient water from x-ray diffraction measurements with a wide Q -range. *The Journal of Chemical Physics*, 138(7):074506, feb 2013.

[39] T. E. Faber and J. M. Ziman. A theory of the electrical properties of liquid metals. *The Philosophical Magazine: A Journal of Theoretical Experimental and Applied Physics*, 11(109):153–173, 1965.

[40] Charles R. Harris, K. Jarrod Millman, Stéfan J. van der Walt, Ralf Gommers, Pauli Virtanen, David Cournapeau, Eric Wieser, Julian Taylor, Sebastian Berg, Nathaniel J. Smith, Robert Kern, Matti Picus, Stephan Hoyer, Marten H. van Kerkwijk, Matthew Brett, Allan Haldane, Jaime Fernández del Río, Mark Wiebe, Pearu Peterson, Pierre Gérard-Marchant, Kevin Sheppard, Tyler Reddy, Warren Weckesser, Hameer Abbasi, Christoph Gohlke, and Travis E. Oliphant. Array programming with NumPy. *Nature*, 585(7825):357–362, sep 2020.

[41] G. Morard, M. Mezouar, S. Bauchau, M. Alvarez-Murga, J.-L. Hodeau, and G. Garbarino. High efficiency multichannel collimator for structural studies of liquids and low-z materials at high pressures and temperatures. *Review of Scientific Instruments*, 82(2):023904, 2011.

[42] Gunnar Weck, Gaston Garbarino, Sandra Ninet, Dylan Spaulding, Frederic Datchi, Paul Loubeyre, and Mohamed Mezouar. Use of a multichannel collimator for structural investigation of low-z dense liquids in a diamond anvil cell: Validation on fluid h2 up to 5 gpa. *Review of Scientific Instruments*, 84(6):063901, 2013.

[43] https://numpy.org/doc/stable/reference/generated/numpy.convolve.html.

[44] Pauli Virtanen, Ralf Gommers, Travis E. Oliphant, Matt Haberland, Tyler Reddy, David Cournapeau, Evgeni Burovski, Pearu Peterson, Warren Weckesser, Jonathan Bright, Stefan J. van der Walt, Matthew Brett, Joshua Wilson, K. Jarrod Millman, Nikolay Mayorov, Andrew R. J. Nelson, Eric Jones, Robert Kern, Eric Larson, CJ Carey, lhan Polat, Yu Feng, Eric W. Moore, Jake Vand erPlas, Denis Laxalde, Josef Perktold, Robert Cimrman, Ian Henriksen, E. A. Quintero, Charles R Harris, Anne M. Archibald, Antonio H. Ribeiro, Fabian Pedregosa, Paul van Mulbregt, and SciPy 1. 0 Contributors. Scipy 1.0: Fundamental algorithms for scientific computing in python. *Nature Methods*, 2020.

[45] J. D. Hunter. Matplotlib: A 2d graphics environment. *Computing in Science & Engineering*, 9(3):90–95, 2007.

[46] Tom Schoonjans, Antonio Brunetti, Bruno Golosio, Manuel Sanchez del Rio, Vicente Armando Sole, Claudio Ferrero, and Laszlo Vincze. The xraylib library for x-ray matter interactions. recent developments. *Spectrochimica Acta Part B: Atomic Spectroscopy*, 66(11):776–784, 2011.

[47] Matthew Newville, Till Stensitzki, Daniel B. Allen, and Antonino Ingargiola. LMFIT: Non-Linear Least-Square Minimization and Curve-Fitting for Python (Version 0.8.0). *Zenodo*, September 2014.

[48] Fredrik Lundh. An introduction to tkinter. *URL: http://jgaltier.free.fr/Terminale$_S$/ISN/TclTk$_I$ntroduction$_T$o$_T$kinter.pdf*, 1999.

[49] F. Decremps, G. Morard, G. Garbarino, and M. Casula. Polyamorphism of a ce-based bulk metallic glass by high-pressure and high-temperature density measurements. *Phys. Rev. B*, 93:054209, Feb 2016.

[50] Bo Zhang, R. J. Wang, D. Q. Zhao, M. X. Pan, and W. H. Wang. Properties of Ce-based bulk metallic glass-forming alloys. *Phys. Rev. B*, 70:224208, Dec 2004.

[51] B. Zhang, M. X. Pan, D. Q. Zhao, and W. H. Wang. Soft bulk metallic glasses based on cerium. *Applied Physics Letters*, 85(1):61–63, 2004.

[52] Guillaume Morard, Denis Andrault, Daniele Antonangeli, and Johann Bouchet. Properties of iron alloys under the earth's core conditions. *Comptes Rendus Geoscience*, 346(5-6):130 – 139, 2014.

[53] A. Dewaele, A. B. Belonoshko, G. Garbarino, F. Occelli, P. Bouvier, M. Hanfland, and M. Mezouar. High-pressure-high-temperature equation of state of KCl and KBr. *Physical Review B - Condensed Matter and Materials Physics*, 85(21):1–7, 2012.

[54] Andrew J Campbell, Lisa Danielson, Kevin Righter, Christopher T Seagle, Yanbin Wang, and Vitali B Prakapenka. High pressure effects on the iron - iron oxide and nickel - nickel oxide oxygen fugacity buffers. *Earth and Planetary Science Letters*, 286(3-4):556–564, 2009.

[55] Clemens Prescher and Vitali B. Prakapenka. DIOPTAS : a program for reduction of two-dimensional X-ray diffraction data and data exploration. *High Pressure Research*, 35(3):223–230, jul 2015.

[56] Yasuhiro Kuwayama and Kei Hirose. Phase relations in the system FeFeSi at 21 GPa. *American Mineralogist*, 89:273–276, 2004.

[57] Sylvain Petitgirard, Wim J. Malfait, Ryosuke Sinmyo, Ilya Kupenko, Louis Hennet, Dennis Harries, Thomas Dane, Manfred Burghammer, and Dave C. Rubie. Fate of mgsio3 melts at core–mantle boundary conditions. *Proceedings of the National Academy of Sciences*, 112(46):14186–14190, 2015.

[58] Yoshio Kono, Yuki Shibazaki, Curtis Kenney-Benson, Yanbin Wang, and Guoyin Shen. Pressure-induced structural change in mgsio3 glass at pressures near the earth's core–mantle boundary. *Proceedings of the National Academy of Sciences*, 115(8):1742–1747, 2018.

[59] Philip S. Salmon, Gregory S. Moody, Yoshiki Ishii, Keiron J. Pizzey, Annalisa Polidori, Mathieu Salanne, Anita Zeidler, Michela Buscemi, Henry E. Fischer, Craig L. Bull, Stefan Klotz, Richard Weber, Chris J. Benmore, and Simon G. MacLeod. Pressure induced structural transformations in amorphous mgsio3 and casio3. *Journal of Non-Crystalline Solids: X*, 3:100024, 2019.

[60] C.D. Yin, M. Okuno, H. Morikawa, and F. Marumo. Structure analysis of mgsio3 glass. *Journal of Non-Crystalline Solids*, 55(1):131–141, 1983.

[61] Akihiro Yamada, Yanbin Wang, Toru Inoue, Wenge Yang, Changyong Park, Tony Yu, and Guoyin Shen. High-pressure x-ray diffraction studies on the structure of liquid silicate using a paris-edinburgh type large volume press. *Review of Scientific Instruments*, 82(1):015103, 2011.

[62] Sylvain Petitgirard, Wim J. Malfait, Baptiste Journaux, Ines E. Collings, Eleanor S. Jennings, Ingrid Blanchard, Innokenty Kantor, Alexander Kurnosov, Marine Cotte, Thomas Dane, Manfred Burghammer, and David C. Rubie. Sio2 glass density to lower-mantle pressures. *Physical Review Letters*, 119(21):215701, nov 2017.

[63] Nobumasa Funamori, Shino Yamamoto, Takehiko Yagi, and Takumi Kikegawa. Exploratory studies of silicate melt structure at high pressures and temperatures by in situ x-ray diffraction. *Journal of Geophysical Research: Solid Earth*, 109(B3), 2004.

[64] Yoshio Kono, Yu Shu, Curtis Kenney-Benson, Yanbin Wang, and Guoyin Shen. Structural evolution of sio_2 glass with si coordination number greater than 6. *Phys. Rev. Lett.*, 125:205701, Nov 2020.

[65] E. Boulard, A. King, N. Guignot, J.-P. Deslandes, Y. Le Godec, J.-P. Perrillat, A. Clark, G. Morard, and J.-P. Itié. High-speed tomography under extreme conditions at the psiche beamline of the soleil synchrotron. *Journal of Synchrotron Radiation*, 25(3):818–825, 2018.

[66] N. Guignot, A. King, and E. Boulard. Synchrotron x-ray computed microtomography for high pressure science. *Journal of Applied Physics*, 127(24):240901, 2020.

[67] Yusheng Zhao, Robert B. Von Dreele, Donald J. Weidner, and David Schiferl. P- v- t data of hexagonal boron nitride h bn and determination of pressure and temperature using thermoelastic equations of state of multiple phases. *High Pressure Research*, 15(6):369–386, 1997.

[68] Masanori Matsui, Stephen C. Parker, and Maurice Leslie. The MD simulation of the equation of state of MgO: Application as a pressure calibration standard at high temperature and high pressure. *American Mineralogist*, 85(2):312–316, 02 2000.

[69] Masanori Matsui, Eiji Ito, Tomoo Katsura, Daisuke Yamazaki, Takashi Yoshino, Ayako Yokoyama, and Ken-ichi Funakoshi. The temperature-pressure-volume equation of state of platinum. *Journal of Applied Physics*, 105(1):013505, 2009.

[70] Daijo Ikuta, Yoshio Kono, and Guoyin Shen. Structural analysis of liquid aluminum at high pressure and high temperature using the hard sphere model. *Journal of Applied Physics*, 120(13):135901, 2016.

[71] Noel Jakse and Alain Pasturel. Liquid aluminum: Atomic diffusion and viscosity from ab initio molecular dynamics. *Scientific Reports*, 3(1):2045–2322, 2013.

[72] D. J. González, L. E. González, J. M. López, and M. J. Stott. Dynamical properties of liquid al near melting: An orbital-free molecular dynamics study. *Phys. Rev. B*, 65:184201, Apr 2002.

[73] Yuki Shibazaki and Yoshio Kono. Effect of silicon, carbon, and sulfur on structure of liquid iron and implications for structure-property relations in liquid iron-light element alloys. *Journal of Geophysical Research: Solid Earth*, 123(6):4697–4706, 2018.

[74] C Sanloup, G Fiquet, E Gregoryanz, G Morard, and M Mezouar. Effect of Si on liquid Fe compressibility : Implications for sound velocity in core materials. *Geophysical Research Letters*, 31(L07604):1–4, 2004.

[75] Ryuji Tateyama, Eiji Ohtani, Hidenori Terasaki, Keisuke Nishida, Yuki Shibazaki, Akio Suzuki, and Takumi Kikegawa. Density measurements of liquid Fe-Si alloys at high pressure using the sink-float method. *Physics and Chemistry of Minerals*, 38(10):801–807, 2011.

[76] N. W. Ashcroft and David C. Langreth. Structure of binary liquid mixtures. i. *Phys. Rev.*, 156:685–692, Apr 1967.

[77] Chrystèle Sanloup, Drewitt Jwe, Crépisson C., Kono Y., Park C., Mccammon C., Hennet L., Brassamin S., and Bytchkov A. Structure et la densité de fayalite fondu à haute pression. *Geochimica et Cosmochimica Acta*, 118:118–128, 2013.

Sec.	Sample	Conditions	Technique	Results
4.1	$Ce_{70}Al_{10}Ni_{10}Cu_{10}$ solid amorph. alloy	amb P, amb T	ADXRD in DAC	S(Q), g(r), ρ_0, χ^2 contour plot with χ^2 [c]
4.2	liquid metal Fe	40 GPa, 4800 K	ADXRD in DAC	S(Q), g(r), ρ_0
4.3	$MgSiO_3$ solid amorph. alloy	2 - 80 GPa, 300 K	ADXRD in DAC with MC	S(Q), g(r), ρ_0 for all data with Batch [b]
4.4	SiO_2 solid amorph. alloy	amb P, amb T	CAESAR in UToPEC	S(Q), g(r)
4.5	liquid metal Al	1.5 - 2 GPa, 1200 - 1350 K	CAESAR in UToPEC	S(Q), g(r), ρ_0
4.6	liquid alloy Fe-Si	7 GPa, 1990 K	CAESAR in MA	S(Q), g(r), ρ_0

Table 1.: Summary of scientific examples presented in this work. ADXRD indicates angular dispersive X-ray diffraction, while CAESAR is a combination of angular and energy dispersive x-ray diffraction (for details see [11, 12]). With DAC, UToPEC and MA we refer to experiments respectively performed in Diamond Anvil Cell, in Ultrafast Tomography Paris Edinburgh Cell [65, 66], and in Multi-Anvil press. With MC we refer to the Multichannel Collimator [41, 42].

P (GPa) - T(K)	q1 (nm^{-1}) /(height)	q2 (nm^{-1})	q3 (nm^{-1})	q4 (nm^{-1})
1.5 - 1200	26.9 /(2.46)	49.4	73.3	98.6
2 - 1350	26.9 /(2.38)	49.6	73.4	99.3

P (GPa) - T(K)	r1 (nm) /(height)	r2 (nm)	r3 (nm)
1.5 - 1200	0.277 /(2.87)	0.513	0.745
2 - 1350	0.276 /(2.82)	0.513	0.746

Table 2.: Liquid Al: peak positions of S(Q) and g(r) shown in Figure 12.

	[Parameters]
[1]	Filename = Cerium.dat
[2]	Filename background = Background.xy
[3]	File Format = 4
[4]	incoherent (1 on empty cell, 0 on sample) = 1
[5]	lambd (nm) = 1
[6]	qmin (nm-1) = 15
[7]	qmax (nm-1) = 78
[8]	rmin (nm) = 0.22
[9]	bkfactor = 0.92737
[10]	rhomi (at/nm3) = 34.68
[11]	Normalization Type = 0
[12]	SofQ = 1
[13]	QStep = 0
[14]	Normalization save filename = Norm
[15]	Loop over rmin save filename = MinRmin
[16]	Loop over qmax save filename = MinQmax
[17]	Elements = ['Ce', 'Al', 'Ni', 'Cu', 'Fe', 'C']
[18]	Content = [0.7 0.1 0.1 0.1 0. 0.]

Table 3.: File "Init.txt" with the input parameters.

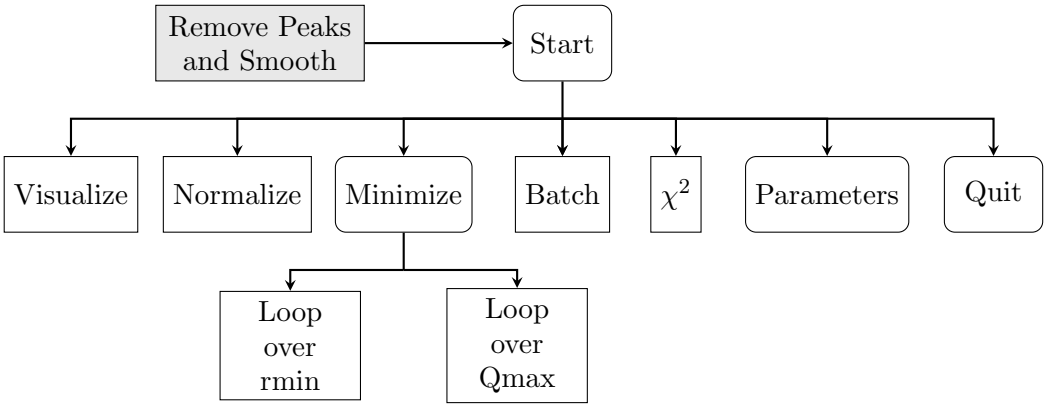


```
/\/\/\/\/\/\/\/\/\/\/\/\/\/\/\/\/\/\/\/\/\/\/\/\/\/\/\/\/\/\/\/\/\/\/\/\/\/\/\/\

Welcome to AMORPHEUS!!


################################################################
#
#  Visualize [v] - Normalize [n] - Loop rmin [r] - Loop qmax [x]
#  Batch [b] - Chi2 [c] - Parameters [p] - Quit [q]
#
################################################################
```

Figure 1.: Top: Functional flowchart of Amorpheus. Bottom: Menu screenshot in Spyder (https://www.spyder-ide.org/). Typing the corresponding letter allows to enter in a specific section of the menu.

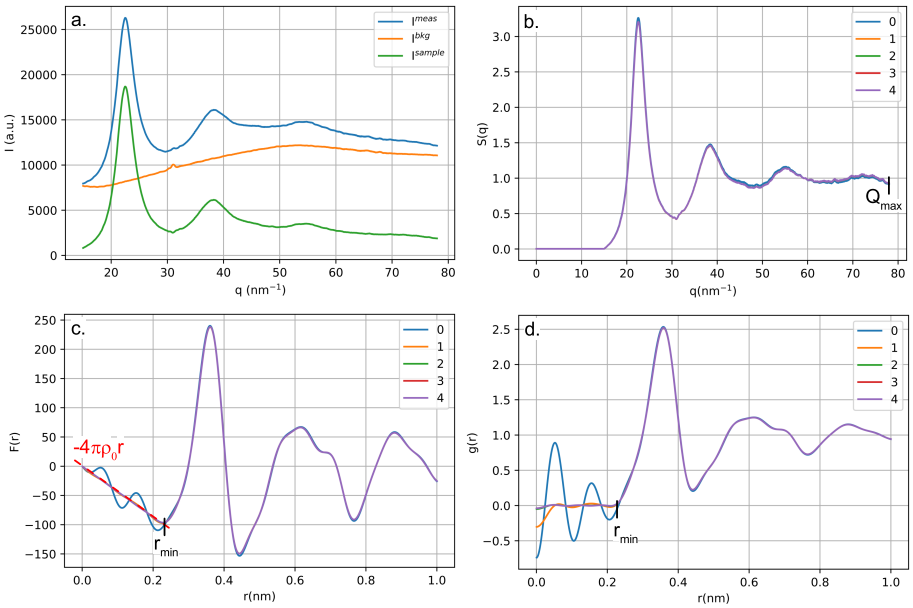

Figure 2.: Normalization of the scattering intensity collected for a Ce-based glass. Panel a. The measured scattering intensity is shown in blue, the background in orange and the contribution of the sample calculated with Equation 1 is shown in green. Panels b., c. and d. show the 5 iterations for $S(Q)$, $F(r)$ and $g(r)$. Convergence is reached already at the third iteration, but 5 iterations are typically used [7]. In panel b. the parameter Q_{max} is evidenced; in panels c. and d. the parameter r_{min}. The red dashed line in panel c. represents the $-4\pi\rho_0 r$ limit to which the distribution function F(r) should converge for distances lower than the cutoff radius $r < r_{min}$ (see Equation 6).

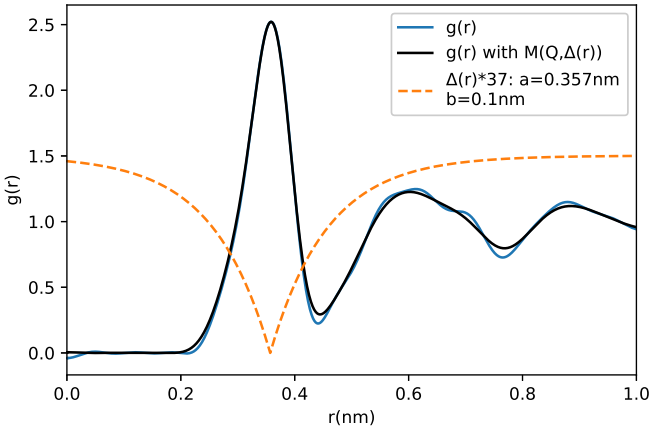

Figure 3.: Effect of modification function on the $g(r)$ of a Ce-based glass. In blue is represented the $g(r)$ as it is calculated with the 5 iterations in the normalization process. The $g(r)$ obtained with the application of the modification function on the $S(Q)$ calculated at the 5-th iteration, $S_5(Q)$, is shown in black. The $\Delta(r)$ function of Equation 9 is shown as a dashed orange line. Parameters a and b of Equation 9 were chosen as $a = 0.357$ nm, close to the position of the first peak of the $g(r)$, and $b = 0.1$ nm, corresponding to about the width of the peak. This choice of parameters leaves unaltered the position and the shape of the first peak, but removes spurious signals in the oscillations, as visible between 0.6 and 0.7 nm.

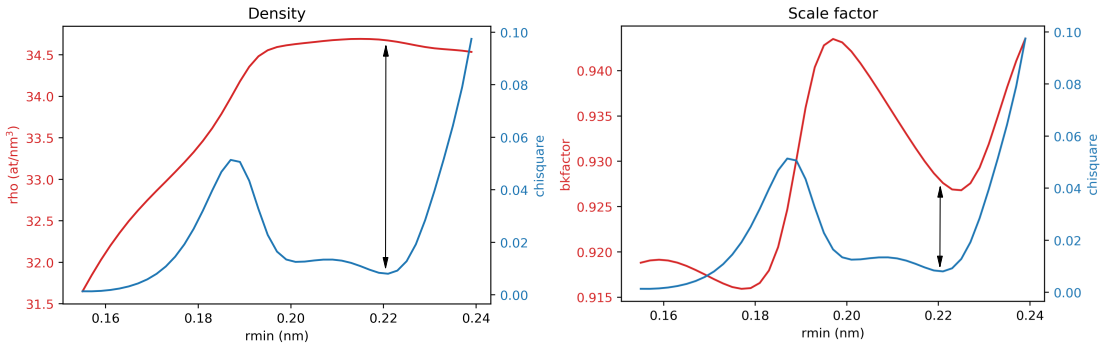

Figure 4.: Loop over rmin for a Ce-based glass at ambient pressure. In blue is shown the value of the chisquare, the figure of merit defined in Equation 8, obtained at the end of each minimization for each value of the cutoff distance. The optimized values for the density and the scale factor are shown in red in the left and right panel respectively. The value of cutoff distance for which the figure of merit is minimized is $r_{min} = 0.221$ nm and the corresponding density and scale factor are $\rho = 34.68$ at/nm^3 and $b = 0.927$.

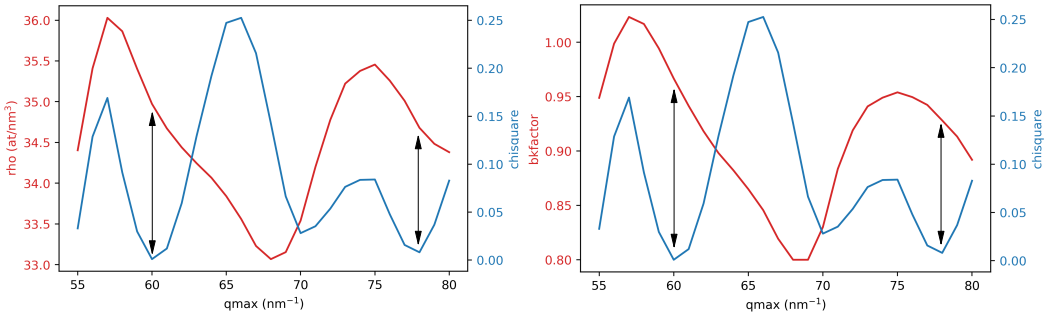

Figure 5.: Loop over qmax for a Ce-based glass at ambient pressure. The minima in the figure of merit (the chisquare, in blue) indicate the preferred values for qmax. The corresponding density (left, in red) and scale factor (right, in red) are the optimized values. In this case there are two possible local minima. One is for Q_{max} = 60 nm^{-1}, with associated ρ = 34.97 at/nm^3 and b = 0.967. The other for Q_{max} = 78 nm^{-1} and ρ = 34.68 at/nm^3 and b = 0.928.

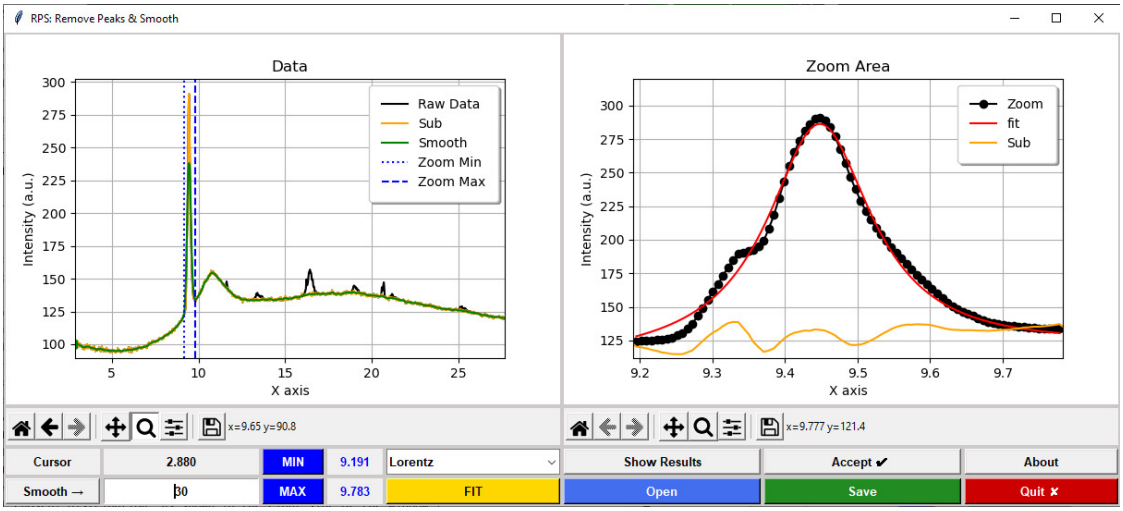

Figure 6.: Screenshot of RPS: Remove Peaks & Smooth program. In the left side of the window is shown in black the Raw Data before any treatment, in orange (Sub) the data after subtraction of the peaks fitted to a chosen distribution function and in green (Smooth) the data after smoothing. The dashed blue vertical lines define the left and right limits for the Zoom of the data to be fit to the chosen distribution function, as shown in the right side of the window.

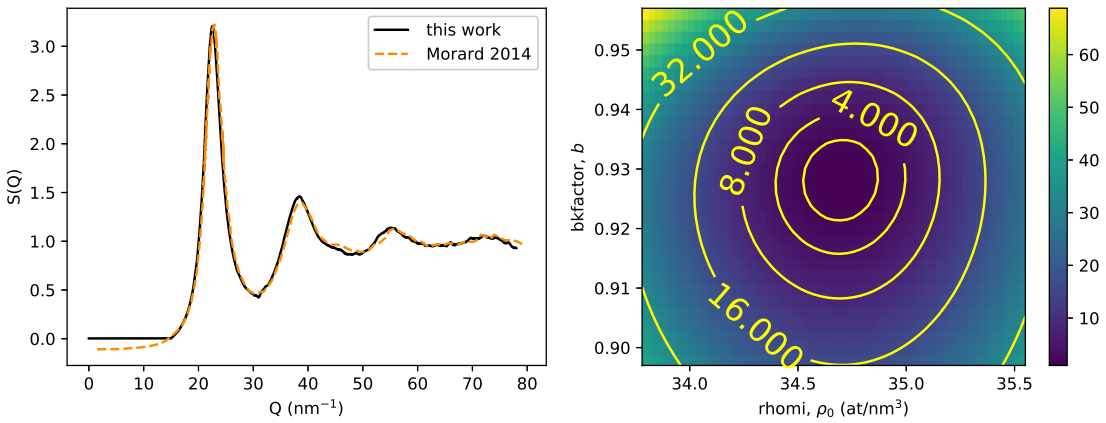

Figure 7.: Left panel: Structure factor of Ce-based glass obtained in this work (black line) and compared to the literature (dashed orange line) [52]. Right panel: χ^2 contour plot as function of density ρ_0 and scale factor b. This calculation was performed choosing Q_{max}=78 nm^{-1} and r_{min}=0.22 nm. χ^2 was normalized to 1 at the minimum, and its normalized value is represented in the colored scale to the right.

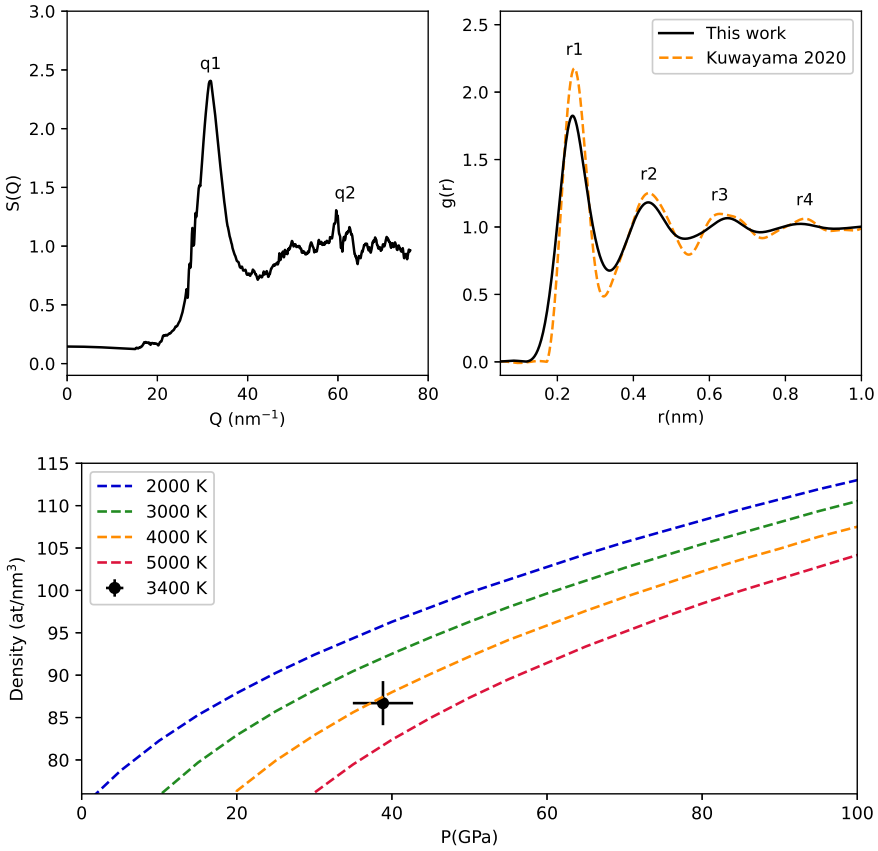

Figure 8.: Top panel: Liquid iron at 38±2 GPa and 3400±300 K. Structure factor and radial distribution function obtained in the Q range between 15 and 76 nm^{-1} and with an rmin = 0.155 nm. In dashed orange line is represented the g(r) reported at 40.7 GPa and 2860 K [20]. Bottom panel: Density obtained in this work (represented by the black dot) compared to the model proposed in literature by Kuwayama et al. (represented by the dashed curves) [20].

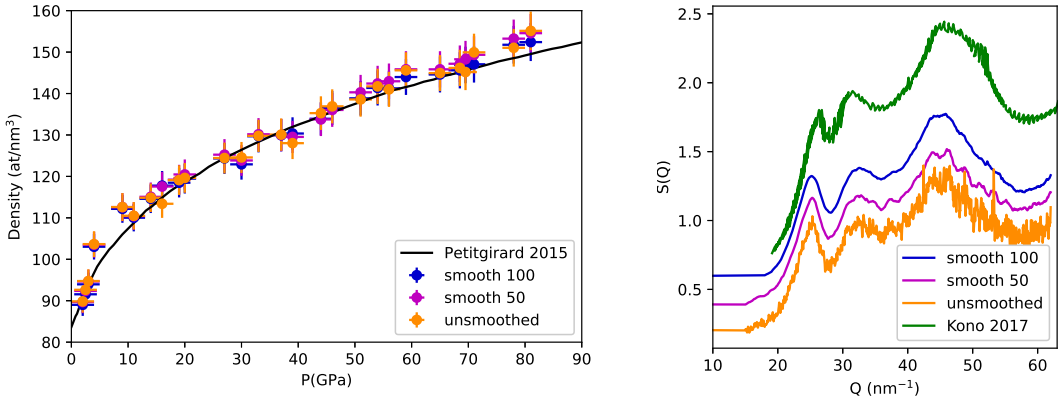

Figure 9.: Left panel: Derived density of $MgSiO_3$ shown as a function of pressure for the same raw data treated by different smoothing approaches. Minimized densities do not depend on the degree of smoothing that has been applied to the data and the derived values are in very good agreement with results from x-ray absorption measurements [57]. Right panel: S(Q) at 27 GPa for signals with different smoothing, compared with the S(Q) reported by Kono et al. [58] at 30 GPa.

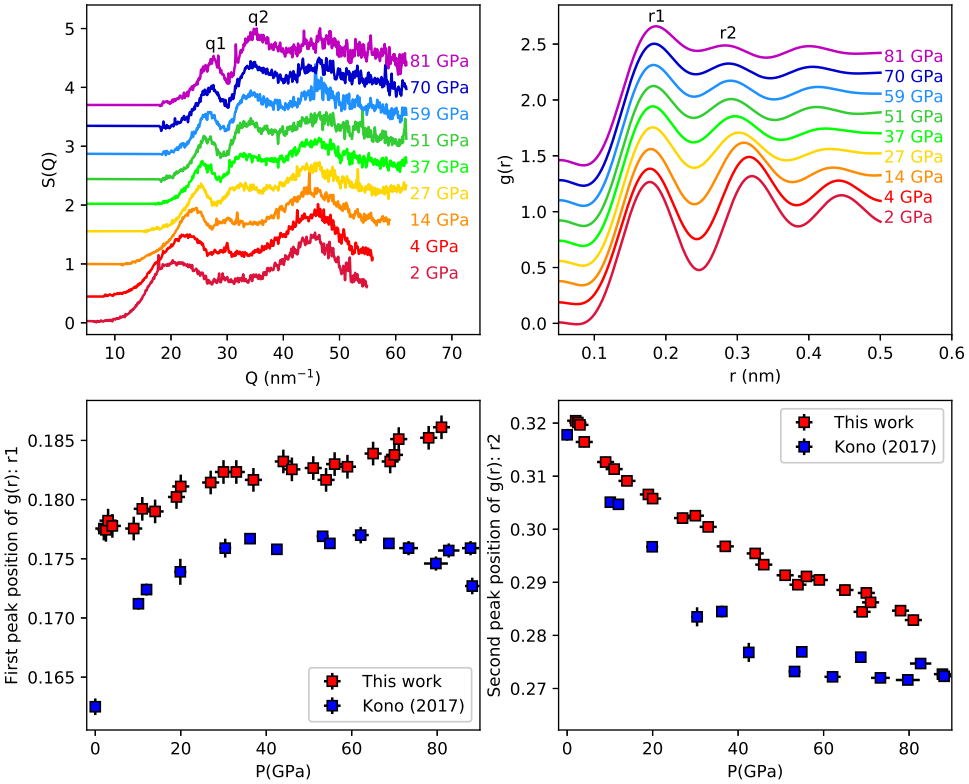

Figure 10.: Pressure dependence of the structure factor (top left panel) and radial distribution function (top right panel) of $MgSiO_3$. The data at different pressures are shown with a vertical offset for clarity of presentation. In the S(Q), the structures designated with q1 and q2 shift to larger Q with pressure and their relative intensity changes. In the g(r), with increasing pressure, the first peak, designated with r1, slightly shifts to larger distances, while peak r2 shifts to shorter distances. The two bottom panels show the comparison of the pressure dependence of r1 and r2 with literature results [58].

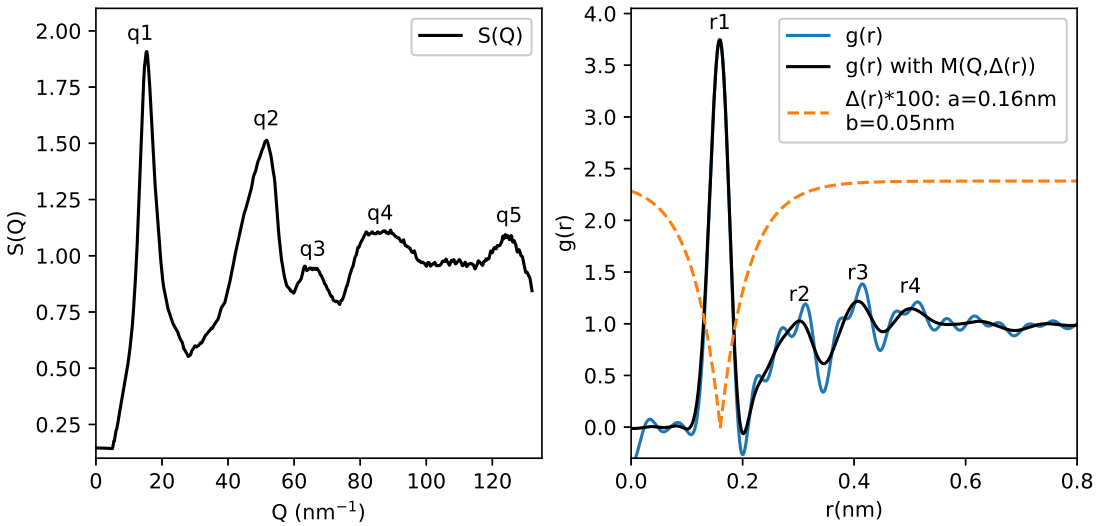

Figure 11.: Structure factor (left) and radial distribution function (right) of SiO_2 glass at ambient pressure and temperature conditions. The positions of the peaks in the S(Q) are: q1 = 13.4 nm^{-1}, q2 = 51.58 nm^{-1}, q3 = 65.63 nm^{-1}, q4 = 86.05 nm^{-1} and q5 = 125.05 nm^{-1}. Right panel: radial distribution function before and after application of the modification function. The peaks positions for the g(r) with modification function are: r1 = 0.159 nm, r2 = 0.302 nm, r3 = 0.407 nm and r4 = 0.501 nm. The Δ(r) function of Equation 9 with a = 0.16 nm and b = 0.05 nm is here multiplied by 100 for visualization purposes.

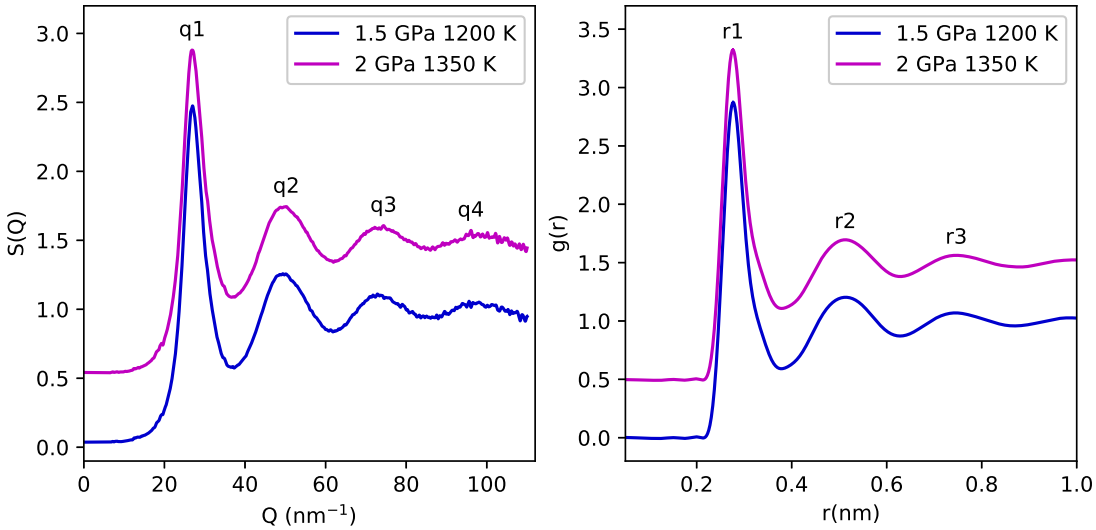

Figure 12.: Structure factor (left panel) and radial distribution function (right panel) of liquid Al at high pressure and temperature. Peaks positions are reported in Table 2.

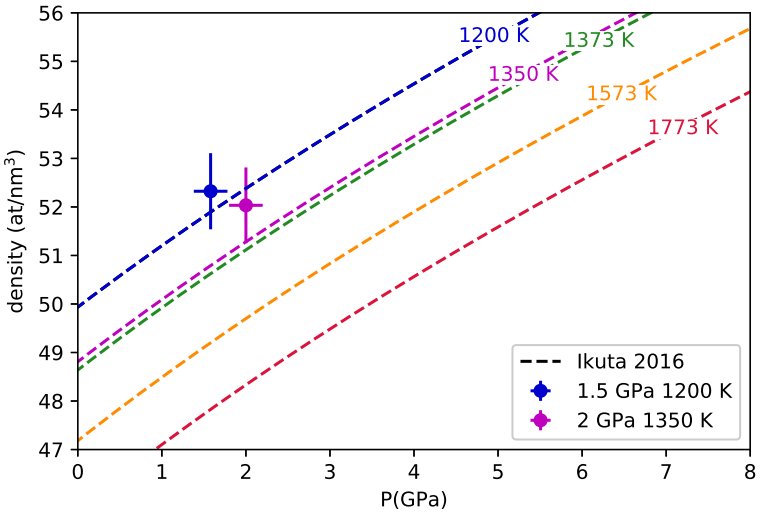

Figure 13.: Densities of liquid Al at high pressure and high-temperature obtained in this work in comparison with the 2nd-order Birch-Murnaghan equation of state reported by Ikuta et al.[70] recalculated at the temperatures pertinent to this work.

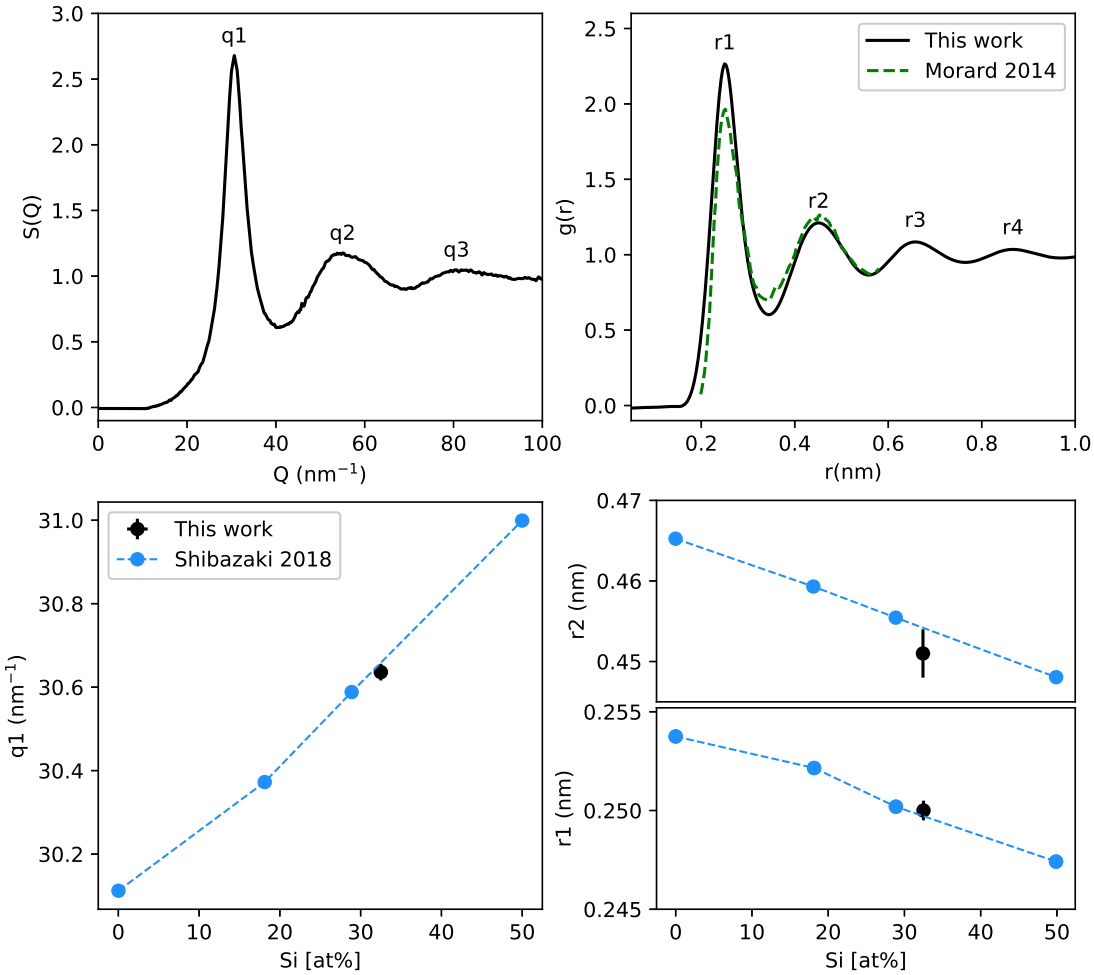

Figure 14.: Top panel: Fe-Si at 7.3 GPa and 1990 K. The structure factor obtained in this work is shown in the top left panel. The g(r) obtained in this work is shown in the top right panel and compared to a g(r) obtained with ab-initio calculation [52]. (translated by 0.011 nm to match the position of the r1 peak). The bottom left panel shows the position of the first peak of the S(Q) as a function of silicon content obtained in this work in comparison with previous determination by x-ray diffraction [73]. Similarly the bottom right panel shows the position of the first two peaks of the radial distribution function as a function of silicon content obtained in this work and compared to the literature [73].